Comparative Study of Silicon Photonic Modulators based on Transparent Conducting Oxide and Graphene

Georgios Sinatkas[1,*] Thomas Christopoulos[1] Odysseas Tsilipakos[2] and Emmanouil E. Kriezis[1]

[1]*School of Electrical and Computer Engineering, Aristotle University of Thessaloniki (AUTH), Thessaloniki 54124, Greece*

[2]*Institute of Electronic Structure and Laser, Foundation for Research and Technology Hellas (FORTH), Heraklion, Crete 71110, Greece*

Transparent conducting oxides (TCOs) and graphene have been extensively investigated as promising materials for electro-optic modulation applications due to their dynamically configurable near-infrared properties. In this study, a detailed comparison between modulators comprising either a TCO film or a graphene-insulator-graphene structure is presented, considering a conventional silicon photonic waveguide as the underlying physical system. Both in-line and resonant configurations are investigated, integrating an electro-optic switching mechanism that changes the free-carrier concentration in the configurable material by means of electrical gating. The carrier-concentration change effect is rigorously modeled using solid-state physics principles, providing a physically consistent and straightforward comparison between the investigated material platforms. The performance of the designed modulators is thoroughly evaluated in terms of the extinction ratio, insertion loss, energy consumption, and bandwidth in both TE and TM operation. On the whole, both technologies support high-performance optical modulation, with TCO designs exhibiting an up to 40% smaller footprint, with their graphene counterparts standing out for their subpicojoule-per-bit performance on a physical system as simple as the employed silicon-wire waveguide. The low insertion losses as well as the impressive over-100-GHz switching speeds suggest both TCOs and graphene as very promising material candidates for future on-chip modulation applications.

I. INTRODUCTION

Advances in material science have largely dictated the recent progress in contemporary nanophotonic technology, bringing novel materials with unprecedented optical properties into the forefront. The successful integration of the latter into standard low-loss photonic waveguides holds promise for a new generation of dynamically configurable components with a reduced footprint and energy consumption and an ultrafast response. Highly electro-optic (EO) polymers [1] and phase-change compounds [2] as well as low-dimensional materials [3,4] have been proposed as potential candidates for achieving enhanced optical control. In this study, two of the most promising material platforms, which have dominated the research on EO modulators in recent years, are carefully reviewed and compared: the transparent-conducting-oxide (TCO) compounds [5–7] and the two-dimensional (2D) graphene monolayer [8,9], both being highly conductive and optically configurable.

Nominally used as conductive transparent electrodes [10], TCOs have regained their popularity for near-infrared (NIR) applications due to their epsilon-near-zero (ENZ) properties, which are tunable through free-carrier concentration changes [11]. State-of-the-art applications include free-space absorbers [12,13] as well as on-chip silicon photonic [14,15] and (hybrid) plasmonic modulators [16–21], controllable using the field effect. In a similar manner, the successful exfoliation of graphene [22] has allowed researchers to envision gate-tunable modulators with one [23–25] or more [26–28] monolayers, capitalizing on the Dirac-band structure of graphene, which provides remarkable carrier mobility and tunable optical conductivity by means of interband transition manipulation.

With the physical principles governing TCO and graphene modulators being essentially alike, this study revisits both material platforms to comparatively assess their modulation potential on common grounds, using a rigorous modeling framework that accurately captures the physics of the underlying effects, avoiding approximate modeling approaches that frequently lack physical rigor or erroneously translate the modulation effect. The application of a common modeling framework in addition to opting for a physically consistent material representation ensures a fair and straightforward comparison between two of the most promising modulation technologies.

*gsinatka@auth.gr

Consequently, an equitable quantitative comparison is achieved, revealing the strengths and weaknesses of each technology, avoiding a comparison based on dissimilar literature calculations.

The comparison is performed on a conventional low-loss silicon photonic waveguide, with an emphasis on amplitude-modulation schemes, where the switching effect is induced by electrically biasing the configurable medium. Indium tin oxide (ITO) is selected as the most mature TCO compound [29], while a graphene-insulator-graphene capacitor structure is exploited for efficiently tuning the graphene conductivity. In-line and resonant configurations attract equal attention, covering the full spectrum of potential modulation schemes. The devices are designed from the ground up using computationally efficient tools that allow for the reduction of complexity without affecting the design accuracy. This is especially important in the case of resonant modulators, where a full three-dimensional (3D) study would require significant computational resources to successfully capture the underlying physical effects, this being particularly prohibitive in the case of bulk TCO materials.

A thorough comparison of the proposed designs in terms of their modulation performance is provided, including the achievable extinction ratio (ER) and insertion-loss (IL) penalty as well as the required energy consumption and allowed bandwidth. The device footprint is minimized by enhancing light-matter interaction through proper geometry engineering, providing a valuable physical insight into the efficient design of TCO and graphene components with respect to the supported mode polarization.

The rest of this paper is structured as follows. In Sec. II, the salient optical properties of TCOs and graphene are reviewed, together with their respective NIR models. Section III presents the underlying physical systems for developing the EO modulators, using variants of the conventional silicon photonic waveguide. Both in-line and microring modulation designs are described in Secs. IV and V, respectively, with their energy requirements and speed limitations evaluated in Sec. VI. An overall comparison among the designed modulators is presented in Sec. VII, together with a discussion on the most recent experimental results. The study is performed using COMSOL Multiphysics®, adopting the $\exp(j\omega t)$ time-harmonic convention.

II. NEAR-INFRARED MATERIAL PROPERTIES

A key attribute of both TCOs and graphene is their tunable carrier-dependent NIR properties. The level of free carriers in TCOs ($n \sim 10^{19} - 10^{21}$ cm^{-3}), together with their low background polarizability values ($\varepsilon_\infty \approx 4$), allows their plasma frequency to lie in the NIR, resulting in near-zero permittivity values. This enables $\varepsilon_{\text{TCO}}(n)$ to be tuned from dielectric to metallic values, subject to the

concentration n of free carriers, intermediately crossing a threshold concentration n_{th} where the real permittivity part equals zero (the ENZ region). At this concentration value, TCOs support the so-called *ENZ effect* when integrated in a heterogeneous dielectric stack [Fig. 1(a)], which is manifested through the substantial electric field enhancement for the mode accommodated in the TCO material. This stems from the continuity condition for the normal displacement-field component, becoming more pronounced due to the significantly discontinuous permittivity profile across a material stack containing an ENZ layer. For thin-film layers, the ENZ effect results in the scaling of guided mode loss with $a \propto \text{Im}\{\varepsilon_{\text{TCO}}\}/|\varepsilon_{\text{TCO}}|^2$ [30,31], plotted in Fig. 1(b) for ITO as a function of its electron concentration together with its complex permittivity at 1.55 μm. Due to the high dopant concentration of TCOs, their permittivity can be described using the Drude model $\varepsilon_{\text{TCO}} = \varepsilon_\infty[1 - \omega_p^2/(\omega^2 - j\gamma_{\text{TCO}}\omega)]$, where $\omega_p \propto \sqrt{n}$ and ω are the plasma and operating angular frequency, respectively, and γ_{TCO} the intraband damping rate, which is generally dependent on the dopant and impurity concentration. The Drude parameter values for ITO can be found in Ref. [15]. It is confirmed that the ENZ effect manifests itself near $n_{\text{th}} \approx 6.11 \times 10^{20}$ cm^{-3}, where $\text{Re}\{\varepsilon_{\text{ITO}}\} = 0$, fading for lower (higher)
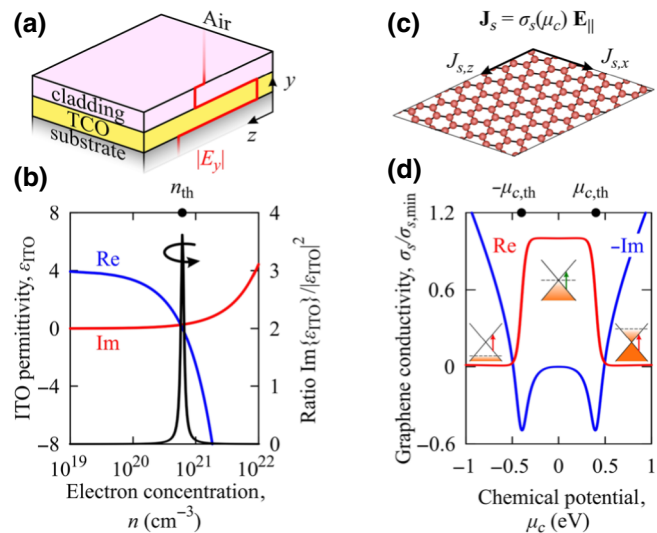

FIG. 1. (a) TCO film sandwiched in a heterogeneous material stack. In the ENZ state, substantial enhancement of the normal E_y component is evidenced (the ENZ effect). (b) The ITO complex permittivity at 1.55 μm as a function of its free-electron concentration. The ratio $a \propto \text{Im}\{\varepsilon_{\text{ITO}}\}/|\varepsilon_{\text{ITO}}|^2$ is also illustrated, peaking at $n_{\text{th}} \approx 6.11 \times 10^{20}$ cm^{-3}. (c) Graphene and its surface current density, induced by the in-plane electric field components. (d) The complex graphene conductivity at 1.55 μm and 300 K as a function of the chemical potential, normalized with respect to $\sigma_{s,\text{min}} = e^2/4\hbar$. A sharp decrease in $\text{Re}\{\sigma_s\}$ is observed at $\mu_{c,\text{th}} = \pm\hbar\omega/2$, signifying the suppression of interband transitions for $|\mu_c| > 0.4$ eV (insets).

electron-concentration values, where the dielectric (metallic) behavior of ITO prevails. The imaginary part of the permittivity, associated with intrinsic material losses, monotonically rises for increasing concentration values.

Next, with reference to Fig. 1(c), the electromagnetic properties of graphene are introduced through a complex surface conductivity, $\sigma_s = \text{Re}(\sigma_s) + j\,\text{Im}(\sigma_s)$, allowing for the consistent interpretation of its 2D nature using a surface-current boundary condition $\hat{\mathbf{n}} \times \Delta\mathbf{H} = \mathbf{J}_s$, where $\hat{\mathbf{n}}$ is the normal vector to the graphene surface and $\Delta\mathbf{H}$ signifies the magnetic field discontinuity across its sides [32]. The latter results from the current density $\mathbf{J}_s = \sigma_s\mathbf{E}_\parallel$ developed on its surface, induced by the tangential electric field components $\mathbf{E}_\parallel$. This modeling approach avoids the frequently applied effective medium representation, which treats graphene as an equivalent bulk material despite its infinitesimal thickness, thus overestimating its effect. The surface conductivity is calculated through

$$\sigma_s(\omega, \mu_c, \tau_{\text{intra}}, \tau_{\text{inter}}, T)$$
$$= \frac{je^2}{\pi\hbar^2(\omega - j\,\tau_{\text{intra}}^{-1})} \int_{-\infty}^{\infty} |\epsilon| \frac{\partial f_d(\epsilon)}{\partial\epsilon}\,d\epsilon$$
$$- \frac{je^2(\omega - j\,\tau_{\text{inter}}^{-1})}{\pi\hbar^2} \int_0^{\infty} \frac{f_d(-\epsilon) - f_d(\epsilon)}{(\omega - j\,\tau_{\text{inter}}^{-1})^2 - 4(\epsilon/\hbar)^2}\,d\epsilon,$$
$$\tag{1}$$

derived from the Kubo formula in the limit of small spatial dispersion [33,34], being in very good agreement with the experimental results as well [35]. The quantities in Eq. (1) are recognized as the elementary charge e, the reduced Planck's constant $\hbar$, and the Fermi-Dirac distribution $f_d(\epsilon) = [e^{(\epsilon - \mu_c)/k_BT} + 1]^{-1}$, with μ_c being the graphene chemical potential (coinciding with the energy difference between the Fermi level and the Dirac point), k_B the Boltzmann constant, and T the lattice temperature. Two separate contributions stand out in Eq. (1), originating from intraband and interband transitions in graphene with electron relaxation times τ_{intra} and τ_{inter}, set equal to 100 fs and 1 ps [36–38], respectively, independent of the energy ϵ. The intraband term $\sigma_{s,\text{intra}}$ can be analytically calculated through

$$\sigma_{s,\text{intra}} = \frac{-je^2 k_B T}{\pi\hbar^2(\omega - j\,\tau_{\text{intra}}^{-1})} \left[\frac{\mu_c}{k_B T} + 2\ln(1 + e^{-\mu_c/k_B T}) \right],$$
$$\tag{2}$$

while $\sigma_{s,\text{inter}}$ requires a numerical computation [39].

In Fig. 1(d), the graphene conductivity at 1.55 μm and $T = 300$ K is illustrated as a function of μ_c, normalized with respect to $\sigma_{s,\text{min}} = e^2/4\hbar$. The exhibited symmetric behavior with respect to $\mu_c = 0$ implies a theoretically identical effect for either electron ($\mu_c > 0$) or hole ($\mu_c < 0$) doping. The real part of the conductivity,

associated with optical losses, decreases sharply at $\mu_{c,\text{th}} = \pm\hbar\omega/2 \approx \pm 0.4$ eV due to Pauli blocking of interband transitions (insets). At the same time, $|\text{Im}\{\sigma_s\}|$ rises for $|\mu_c| > |\mu_{c,\text{th}}|$ as the intraband behavior becomes dominant.

III. PHYSICAL SYSTEMS

A standard silicon-on-insulator (SOI) waveguide is selected as the underlying physical system (Fig. 2), being a technologically mature and fabrication-friendly option, while providing significantly lower ILs compared to plasmonic alternatives [6]. The TCO platform [Fig. 2(a)] consists of an n-doped silicon-rib (Si-rib) waveguide with an unetched slab of 30 nm, loaded with a 5-nm insulating hafnium dioxide (HfO$_2$) layer, followed by a 10-nm ITO film. This layered structure forms a capacitorlike n-Si–HfO$_2$–ITO junction, suitable for controlling the electron concentration in ITO by applying a V_a bias between the n-doped Si slab and the ITO layer. The dopant concentrations in Si and ITO are selected to be equal to 10^{18} cm^{-3} and 10^{19} cm^{-3}, respectively. Opting for a high-κ insulating spacer, such as HfO$_2$ [40], enhances the field effect and reduces energy consumption [15]. The structure is finally covered with an HfO$_2$ cladding to allow for narrow silicon-core values, which are favorable for enhancing the light-ITO interaction, while avoiding mode leakage. Instead of the HfO$_2$ cladding, an electromagnetically equivalent high-index material could be selected. The NIR properties of the selected materials are listed in Ref. [15].

In a similar manner, the graphene platform [Fig. 2(b)] employs a silicon-wire (Si-wire) waveguide loaded with a pair of graphene monolayers, separated by a 5-nm HfO$_2$ spacer. The V_a bias is applied between the graphene pair, regulating graphene's optical conductivity by shifting the chemical potential of the upper (bottom) sheet toward
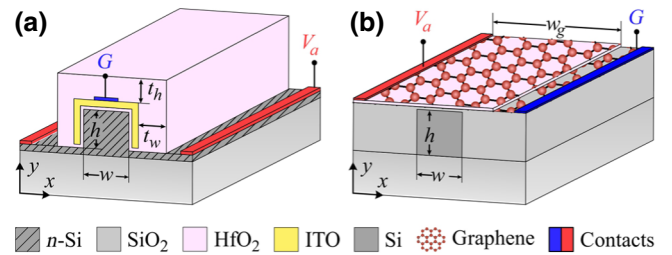

FIG. 2. (a) A silicon-rib waveguide conformally coated by a 5-nm HfO$_2$ layer, followed by a 10-nm ITO film. The structure is clad on top by HfO$_2$ to aid waveguiding. A V_a bias is applied between the n-Si slab and ITO to electro-optically control the guided wave. (b) A silicon-wire waveguide loaded with two graphene monolayers of width w_g, separated by a 5-nm HfO$_2$ spacer. The control bias is applied between the graphene sheets, modulating their conductivity through changes in their carrier density. The ground electrode is denoted with G.

negative (positive) values due to hole (electron) accumulation. Compared with single-graphene platforms [23–25], the investigated double-graphene configuration results in enhanced modulation performance [26–28], not only because of the dual graphene effect but primarily due to its success in homogeneously shifting the chemical potential value along the graphene sheets, as systematically demonstrated in Appendix B.

IV. IN-LINE MODULATORS

Simple in-line modulators are formed by modulating the propagation losses of the waveguides in Fig. 2. Using the field effect to dynamically control the number of free carriers in ITO and graphene, the mode loss can be modulated. Its value can be quantified through the imaginary part of the effective index (n_{eff}) using a conventional mode solver. In order to demonstrate the fundamental on-off shift keying (OOK) scheme, a pair of distinct loss levels are sought, calculated in decibels per micrometer through $a = 20|\log[\exp(-2\pi \text{Im}\{n_{eff}\}/\lambda_0)]|$, with λ_0 denoting the free-space wavelength in micrometers.

In Fig. 3, the mode loss per unit length for both ITO and graphene modulators is illustrated as a function of the applied bias. A steplike behavior is identified for both platforms, exhibiting a V_{th} threshold equal to 2.9 V and 1.2 V for the ITO and graphene designs, respectively, originating from the establishment of ENZ conditions in ITO, $n > n_{th}$, and the suppression of interband transitions in graphene, $|\mu_c| > \mu_{c,\text{th}}$, accordingly. This latent effect is represented

FIG. 4. The electric field components of (a)–(c) the quasi-TE mode and (d)–(f) the quasi-TM mode, in the case of a 400 nm × 220 nm Si-wire waveguide, surrounded by air and lying on top of an SiO_2 substrate. The absolute field values are normalized with respect to the square root of the guided power of each mode.

by the dashed curves in Figs. 3(a) and 3(b), presenting the peak electron-concentration value in ITO (manifested at the ITO-HfO_2 interface) and the absolute value of the graphene chemical potential as functions of V_a, respectively. The field-effect description is presented in detail in Appendix A.

Both TE and TM modes of operation are evaluated, with the geometry of the underlying waveguide being optimally engineered for each polarization to maximize wave interaction with the configurable medium, translated into the shortest length for achieving a performance of ER = 10 dB. Beginning with the ITO modulator, the ENZ effect stems from the electric field components lying *normal* to the ITO film, which are principally the E_x and E_y components for the TE and TM modes, respectively. This can be easily deduced by comparing Fig. 2(a) with the field distributions illustrated in Fig. 4, corresponding to the case of a standard Si-wire waveguide. Correlation of the ENZ effect with a single electric field component allows for optimization of the ITO modulator by examining solely the effect of the w and h parameters on the TE and TM modes, respectively, avoiding an otherwise time-consuming solid-state physics parametric investigation on the entire (w, h) space [15]. The second cross-section parameter for each mode of operation is set equal to a conventional value, Table I. In TE and TM operation, it is $t_w = t_h = 150$ nm and $t_w = t_h/2 = 150$ nm, respectively. On the other hand, graphene modulators capitalize on the interaction between graphene and the *tangential* components of the electric field, E_x and E_z. In TE operation, both of them exhibit increased overlap with the graphene sheets, as evidenced
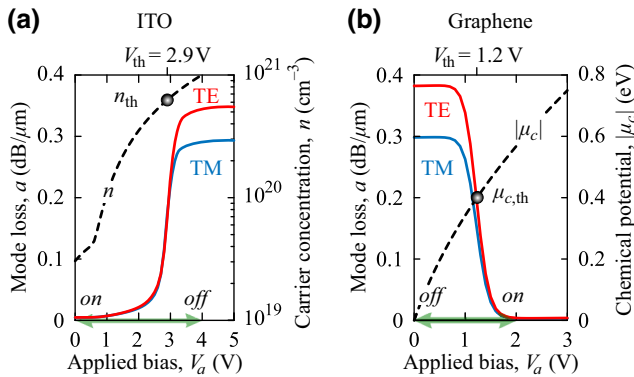

FIG. 3. The mode loss as a function of V_a for (a) ITO and (b) graphene platforms. Both TE and TM modes are investigated, with the underlying waveguide being optimally engineered for each polarization to maximize light-matter interaction. The peak carrier-concentration value in ITO and the chemical potential (absolute value) in graphene are comparatively shown as functions of V_a (dashed lines). A threshold bias V_{th} equal to 2.9 V and 1.2 V is identified for the ITO- and graphene-loaded waveguides, corresponding to the onset of the ENZ effect in ITO, $n \approx n_{th}$, and the suppression of interband transitions in graphene, $|\mu_c| > \mu_{c,\text{th}}$. The green arrows on the horizontal axes indicate the biasing states for achieving the binary loss behavior.
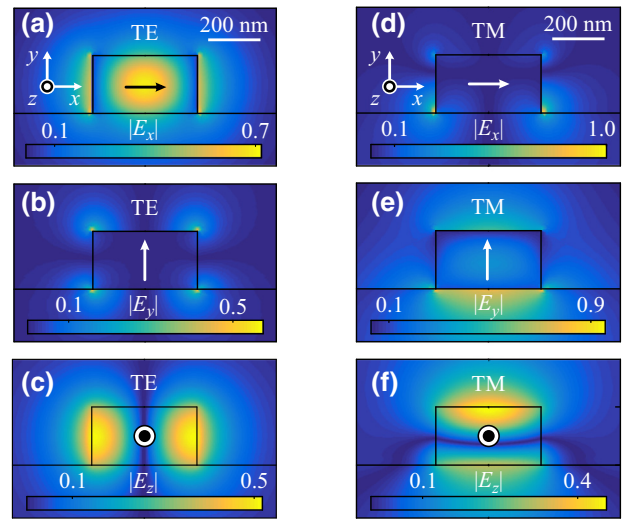
TABLE I.   The transverse dimensions $w \times h$, 10-dB length L, and total IL for ITO and graphene in-line modulators.

Platform	Mode	V_a (V)	$w \times h$ (nm^2)	L (μm)	IL (dB)
ITO	TE	$0 \rightleftarrows 4$	180×220	29	0.14
	TM		400×200	35	0.17
Graphene	TE	$0 \rightleftarrows 2$	400×120	26	0.10
	TM		400×260	34	0.10

from Fig. 2(b) and Figs. 4(a) and 4(c), whereas the interaction with the TM mode is essentially limited to the E_z component, Fig. 4(f). Due to the multiform light-graphene interaction, a full investigation in the (w, h) space is recommended, facilitated computationally by the surface boundary-condition representation of graphene, with the optimal transverse waveguide dimensions listed in Table I.

A preliminary comparison between the two platforms reveals exceptional performance metrics for both TE and TM modes. By allowing V_a to toggle between the unbiased state and 4 V (2 V) for the ITO (graphene) modulator, a 10-dB length equal to a few tenths of micrometers is exhibited in all cases, with the graphene modulator achieving slightly shorter lengths. The IL penalty is calculated around 0.1 dB, with ITO designs suffering from marginally higher loss due to the n-doped Si layer, greatly mitigated, though, by the formation of depletion layers [see Fig. 13(a) in Appendix A]. The TE mode outperforms its TM counterpart in all cases, this being attributed to the double-sided interaction of its E_x component with the ITO layer and its dual-component interaction (E_x and E_z) with graphene.

V. MICRORING MODULATORS

Resonant structures can also be employed for modulation applications by dynamically configuring their resonance and coupling conditions [13,41–45]. In Figs. 5(a) and 5(b), silicon microrings enhanced with ITO and graphene, respectively, modulate the continuous wave (cw) power guided in a side-coupled waveguide from a P_{in} value to the digital output P_{out} under the effect of the applied bias V_a. The microring modulators are studied using a computationally friendly, yet highly reliable, scheme, employing transformation optics in conjunction with a temporal coupled-mode theory (CMT) framework. This approach is preferable compared to a full-wave 3D study in terms of computational resources owing to the significantly fine discretization required for accurately describing the ENZ and graphene effects, which would render a 3D analysis computationally excessive and time inefficient.

Specifically, an axisymmetric 2D mode solver is applied on the optically transformed cross section of the isolated microrings [Figs. 5(c) and 5(d)] to calculate the equivalent n_{eff} of the underlying *bent* waveguide [46–48]. The
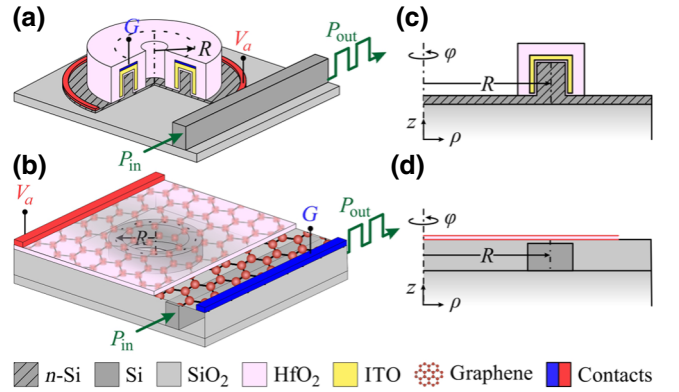

FIG. 5.   (a) ITO and (b) graphene microring modulators. The input cw power P_{in} is modulated to the output power P_{out} by perturbing the resonance and coupling conditions through V_a. A quarter sector of the ITO resonator has been removed to allow for an inner view of its structure, while the underlying resonator in (b) is rendered visible after setting the top layers transparent. (c),(d) Cross sections of the respective isolated 3D resonators, considered in the 2D axisymmetric solver.

resulting Im$\{n_{eff}\}$ encapsulates both resistive and radiation losses, while Re$\{n_{eff}\}$ determines the ring radius R for resonance at $\lambda_0 = 1.55$ μm through

$$R = \frac{m\lambda_0}{2\pi \, \mathrm{Re}\{n_{eff}\}}, \qquad (3)$$

with m denoting the azimuthal resonance mode order. Then, the *intrinsic* quality factor Q_i of the microrings at the resonance wavelength λ_{res} is calculated using [49]

$$Q_i = \frac{\sqrt{a}}{1-a} \frac{\pi n_g L}{\lambda_{res}}, \qquad (4)$$

where $L = 2\pi R$ denotes the round-trip length, $a = \exp[-(2\pi/\lambda_{res})\mathrm{Im}\{n_{eff}\}L]$ is the total loss (resistive and radiation), and $n_g = \mathrm{Re}\{n_{eff}\} - \lambda_{res}\partial\mathrm{Re}\{n_{eff}\}/\partial\lambda$ is the group index. These results are fed to a temporal CMT framework [50–52] to calculate the steady-state transmission at the operating angular frequency ω,

$$T(\omega) \equiv \frac{P_{out}}{P_{in}} = \frac{\delta^2 + (1-r_Q)^2}{\delta^2 + (1+r_Q)^2}, \qquad (5)$$

where $\delta = \tau_i(\omega - \omega_{res})$ denotes the detuning with reference to the resonance frequency ω_{res}, normalized with respect to the intrinsic photon lifetime $\tau_i = 2Q_i/\omega_{res}$, while $r_Q = Q_i/Q_e$ is identified as the quality-factor ratio, with Q_e being the *external* quality factor, related to the external power coupled to the transmitted wave through the microring resonator.

On resonance ($\omega = \omega_{res}$) and for critical coupling conditions ($r_Q = 1$), transmission drops to zero, a stand-out

TABLE II. Design specifications and performance metrics for ITO and graphene microring modulators, including the quality-factor ratio r_Q and detuning $\delta_0 = \tau_i(\omega_0 - \omega_{\text{res}})$ values at their low-loss state, corresponding to the unbiased state of ITO and the 2-V biased state of graphene.

Platform	Mode	m	V_a (V)	$w \times h$ (nm^2)	R (μm)	Q_e	r_Q	δ_0	IL (dB)
ITO	TE	15	$0 \rightleftarrows 4$	400×220	1.4530	438	21	18	0.48
	TM	13		400×220	1.4136	258	25	14	0.54
Graphene	TE	14	$0 \rightleftarrows 2$	440×200	1.5423	350	30	−10	0.53
	TM	14		500×300	1.4889	369	32	−11	0.48

feature in traveling-wave resonant schemes. The condition $r_Q = 1$ is achieved for a suitably selected coupling gap between the resonator and the bus waveguide—requiring, however, a 3D analysis for its calculation. Nevertheless, admitting the existence of a gap value such that $r_Q = 1$ at the design frequency, Eq. (5) allows for modulation of the transmission by perturbing the critical coupling conditions ($r_Q \neq 1$). On the grounds of constant Q_e (fixed gap value), r_Q can be exclusively modified by means of Q_i, which is electrically tunable through field-effect changes in the intrinsic resonator properties. These changes are bound to affect both Re{n_{eff}} and Im{n_{eff}} of the bent waveguide, affecting the resonance frequency and line width, respectively, and thus both δ and r_Q in Eq. (5). As a result, transmission at ω_0 rises from $T_{\text{low}} = 0$ to T_{high}, resulting in a theoretically infinite ER and an IL level equal in decibels to $10|\log T_{\text{high}}|$.

Based on the binary loss behavior evidenced in Fig. 3, the Q_i factor of ITO and graphene resonators can be significantly modified by switching V_a to either side of V_{th}, modulating the intrinsic resistive losses. The geometric parameters maximizing the resistive-loss step across V_{th} have already been identified in Sec. IV for the case of in-line modulators, ensuring optimal interaction of the configurable medium with both TE and TM modes, compensating for the discrepancy in their field maps. However, the additional mechanism of radiation loss in microrings is proven detrimental to the overall intrinsic resonator loss, especially at the desired small-radii values (approximately 1 μm), shrinking the attainable r_Q range and resulting in prohibitive IL values. As a result, the cross-section geometry of microrings has to be properly engineered to account for the extra loss mechanism of radiation. Instead of an exhaustive, multiparametric optimization of the microring geometry, a constraint-oriented approach is preferred, targeting the fulfilment of specific requirements, compatible with state-of-the-art performance metrics. Specifically, radii values as great as 1.5 μm are targeted, ensuring microrings of reduced footprint and energy consumption, with IL restricted to about 0.5 dB.

Starting from the cross-section dimensions of in-line designs, microrings are engineered by iteratively adjusting the silicon-core dimensions $w \times h$ until the desired requirements are met. Table II compiles the design specifications for both material platforms and modes of operation, while Fig. 6 illustrates the respective field profiles, exhibiting a radial shift under the bending effect, as anticipated. An increase in the silicon-core dimensions is necessary in all cases to achieve stronger confinement of the resonance mode, allowing in turn for a reduction in radius due to higher Re{n_{eff}} [Eq. (3)] and a decrease in IL owing to higher r_Q [Eq. (5)]. The compromise between footprint and IL requirements allows for microring Q factors as high as 12 000, which pose no limitation to the cavity dynamics, as discussed in Sec. VI.

The spectral response of the microring modulators is illustrated in Fig. 7 for both biasing states and modes of operation. Resonators are designed to be critically coupled at 1.55 μm and at their high loss state, as also inferred by the low Q_e values listed in Table II. This ensures a relatively small coupling gap with the side coupled waveguide and it provides increased fabrication tolerance as a result of the broad resonance. Switching to the low-loss state renders the resonators overcoupled ($r_Q > 1$), raising the transmission level to T_{high}. This is also evidenced in Fig. 8, where $T(\omega_0)$ is represented as a function of V_a together with the respective change in r_Q and δ_0 for the TE mode. The detuning δ_0 is calculated between the design frequency ω_0 and the bias-dependent resonance frequency ω_{res}, normalized each time with the respective τ_i. As evidenced, the $T(\omega_0)$ behavior is primarily dictated by the r_Q trend and additionally affected by the increasing $|\delta_0|$ values as a result of the resonance shift due to concurrent changes in Re{n_{eff}}. The detuning in ITO microrings results
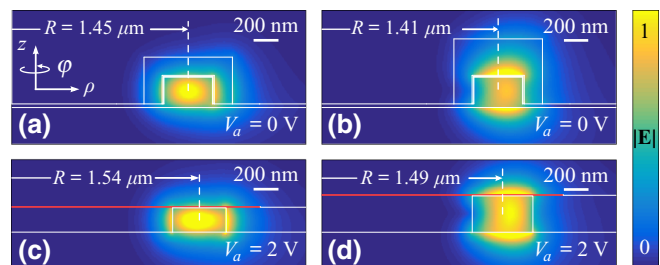

FIG. 6. The TE (left) and TM (right) normalized |**E**|-field distributions for ITO (top) and graphene (bottom) microrings. Their radii and biasing conditions are also indicated.
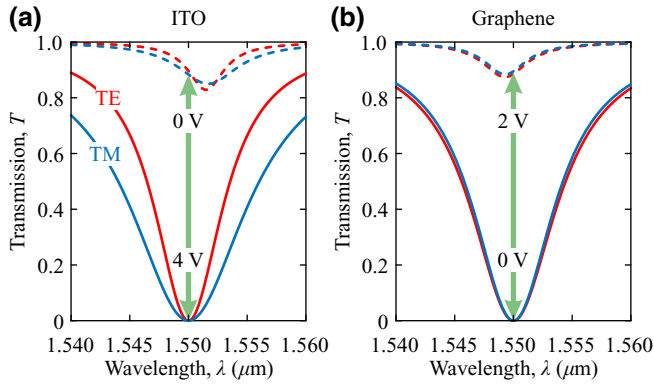
FIG. 7.   The spectral transmission response for (a) ITO and (b) graphene microring modulators in both TE and TM operation. At 1.55 μm, ITO (graphene) resonators are critically coupled ($T_{\text{low}} = 0$) under a 4 V (0 V) bias, switching to an overcoupled state (T_{high}) for 0 V (2 V), respectively.

from the carrier effects in both ITO and Si, constructively contributing to the resonance shift. Positive (negative) δ_0 values red shift (blue shift) the resonance, as also evidenced in Fig. 7. Similar conclusions hold for the omitted TM mode.

All designs achieve a theoretically infinite ER, with an IL penalty around 0.5 dB in both modes of operation. Truly micrometer radii around 1.5 μm are attained, which are highly desirable for achieving a reduced footprint and thus reduced energy consumption. Both modes of operation exhibit almost identical performance due to sharing the same modulation principle, with their respective microring geometries being, in addition, suitably engineered to adhere to common performance criteria. In general, the TM mode exhibits a greater tolerance toward bending, implied by the lower radii values in addition to the required less pronounced deviations of its resonator cross-section geometry from the cross-section geometry of
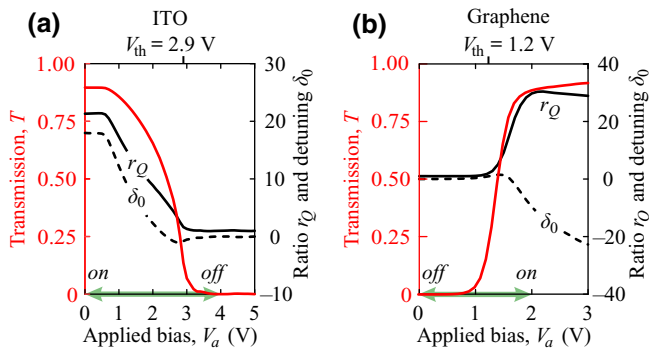

FIG. 8.   The transmission at 1.55 μm for (a) ITO and (b) graphene microring modulators as a function of V_a in TE operation (the TM curves are almost identical). The respective changes in r_Q and δ_0 are also included.

the respective optimal in-line designs (Table I). Biasing conditions identical to the in-line designs are employed for microring modulators, although graphene designs could benefit in terms of IL from the increased detuning values at higher V_a [Fig. 8(b)], which balance out the respective slight fall in r_Q. The latter results from an increase in graphene conductivity due to the resonance blue shift.

VI. BANDWIDTH AND ENERGY REQUIREMENTS

Bandwidth limitations and energy dissipation arise as a result of the total system inertia and the charge-discharge cycles of the control mechanism, respectively. The energy consumption per bit in an equiprobable two-state field-effect modulator can be calculated through $W_b = 1/4 \times W_d$, where W_d denotes the dissipated energy during a complete charge-discharge cycle [53,54]. W_d equals twice the stored energy $W_e = \int_Q V_c \, dq$ in the capacitive structure, with V_c denoting the electrical potential difference between the electrodes (coinciding with V_a in the case of homogeneous junctions) and dq signifying the infinitesimal change in the total charge $Q = \int_\Omega \rho \, d\Omega$, where ρ is the space charge density in the semiconductor volume Ω. Since the examined ITO modulators remain cross-sectionally invariant, the total charge can be equivalently expressed as $Q = L \int_S \rho \, dS$, where L is the modulation length and S the cross section of the underlying waveguide. Alternatively, the field-based formulation described in Ref. [55] could be applied, introducing an extra energy term to account for the generated space charge regions in semiconductors. Similarly, the stored energy in the one-dimensional (1D) graphene-insulator-graphene (GIG) junction takes the form $W_e = \int_{Q_s} V_{\text{ins}} \, dq + 2Q_s(\mu_c/e)$, where Q_s is the graphene surface charge, μ_c is the respective chemical potential shift, and V_{ins} is the voltage drop across the insulator. The surface charge equals $Q_s = \rho_s \times A$, where ρ_s is the surface charge density and $A = L \times w_g$ is the area of graphene. Equivalently, the electrical circuit equivalent of the 1D GIG junction yields $W_e = 1/2 \times [C_g V_{\text{ins}}^2 + 2C_q(\mu_c/e)^2]$, where C_g and C_q are the geometric and quantum graphene capacitance [56], respectively (see Appendix A). Note that no energy-recovery circuit [53] is considered during the calculations, which thus correspond to the upper energy-consumption limit.

The energy consumption scales proportionally to the modulation length, $W_b \propto L$, and the graphene area, $W_b \propto A$, for ITO and graphene modulators, respectively. In Fig. 9(a), the energy consumption per unit length and square area is presented for ITO and graphene modulators, respectively. From an electrostatic standpoint, three distinct n-Si–HfO$_2$–ITO capacitor configurations are identified through Tables I and II in terms of cross-section dimensions, whereas the consumption for all graphene modulators results from evaluating the commonly shared
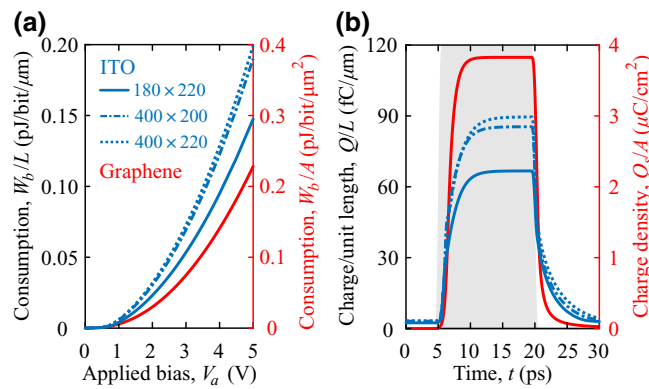
FIG. 9. (a) The energy consumption per bit as a function of the applied bias for ITO and GIG junctions, expressed per unit length and unit area, respectively. (b) The charge-discharge cycle in ITO (graphene) junctions under the application of a 4-V (2-V) rectangular pulse, with a 10%–90% rise time of approximately 0.5 ps (shaded area).

1D graphene-HfO$_2$-graphene structure. Multiplying the calculations in Fig. 9(a) with the modulation length (ring circumference) of ITO in-line (microring) modulators and the area of the GIG junction in graphene designs, the energy consumption per bit is retrieved in Table III. Realistic graphene sheets as wide as 1 μm are considered for in-line modulators, limiting the energy dissipation compared to the theoretical infinite-sheet geometry, while leaving the modulation performance unaffected. Similarly, the sheets in the graphene microring modulators extend as far as half a micrometer away from the Si-core center, requiring an area coverage of at least $\pi(R + 0.5 \ \mu m)^2$. Reviewing the results in Table III, both material platforms limit their energy requirements to picojoule-per-bit values, with graphene designs achieving subpicojoule-per-bit performance due to their requirement for lower biasing swings. The microring modulators are found to be more efficient than their in-line counterparts due to their reduced footprint values, with the latter calculated as the top-viewed occupied area. In terms of mode operation, the TE mode is proven favorable for in-line geometries, providing reduced energy requirements due to reduced footprint values, associated with the stronger interaction between the TE mode and ITO or graphene as described in Sec. IV. On the other hand, microring modulators exhibit an almost polarization-independent performance, enjoying equally low energy requirements for approximately equal footprint values. This similarity is attributed to the common design principle governing both modes of operation (switching between critically and noncritically coupled resonance states) together with the constraint-oriented approach, which requires the fulfilment of common performance specifications from both modes.

Ultrahigh switching speeds, well in excess of 100 GHz, are estimated for both material platforms. Beginning with the in-line designs, their speed is solely limited by the dynamics of the switching mechanism. For the ITO modulators, the temporal response of each n-Si–HfO$_2$–ITO junction is evaluated by solving the time-dependent form of the pertinent differential equation system [15], considering the application of a 4-V rectangular pulse with a 10%–90% rise time of approximately 0.5 ps. Based on the resulting charge-discharge cycles of Fig. 9(b), switching speeds around 100 GHz are estimated using the relation $B = (t_d + t_r + t_s + t_f)^{-1}$, where t_d is the delay time from the pulse application to 10% of the saturation value, t_r is the subsequent 10%–90% rise time, t_s is the storage time from the pulse shutdown to 90% of the saturation value, and t_f is the 90%–10% fall time. Note that the temporal response in Fig. 9(b) could have been equivalently employed for calculating the energy consumption per bit using the relation $W_b = 1/4 \int V_c |I| \, dt$, with $I = dQ/dt$ denoting the electric current flowing during a complete charge-discharge cycle.

TABLE III. A comprehensive comparison among in-line and microring modulators employing the ITO or graphene platform in terms of their IL, footprint, energy consumption, and bandwidth. All in-line modulators are designed to achieve a 10-dB ER, while their microring counterparts enjoy a theoretically infinite ER value.

Design	Platform	Mode	IL (dB)	Footprint (μm^2)	pJ/bit	GHz
In-line (ER = 10 dB)	ITO	TE	0.14	15	2.8	168
		TM	0.17	26	4.3	435[a]
	Graphene	TE	0.10	26	0.8	280
		TM	0.10	34	1.0	280
Microring (ER → ∞)	ITO	TE	0.48	10	1.2	114
		TM	0.54	10	1.1	265[a]
	Graphene	TE	0.53	13	0.4	193
		TM	0.48	12	0.4	191

[a]The performance is attributed to the proximity of the ENZ-active interface to the ground electrode.

Similarly, the temporal response of the GIG junction is evaluated by considering the conventional differential capacitor equation, additionally introducing the quantum-capacitance effect in graphene,

$$\frac{dQ_s(t)}{dt} = \frac{1}{R(t)}\left[V_a(t) - 2\mu_c(t)/e - \frac{Q_s(t)}{C_g}\right]. \quad (6)$$

The total resistance $R = R_{sq}w_gL$ is estimated based on the graphene sheet resistance per square R_{sq}, admitting a contact distance from the Si-core center equal to half the sheet width w_g. The sheet length L is eventually eliminated in the RC time-constant expression, resulting in $RC \propto w_g^2$. The sheet resistance per square is calculated as $R_{sq} = (en_e\mu_e)^{-1}$, where $n_e = 2/\pi\hbar^2v_F^2\int_0^\infty \epsilon f_d(\epsilon)\,d\epsilon$ is the *carrier* density and μ_e is the respective mobility, estimated through a model derived from Ref. [57]. Specifically, a mobility value as high as $20\,000$ cm^2/(V s) is considered for $n_e < 10^{13}$ cm^{-2}, limited by phonon scattering in HfO$_2$ at room temperature and further decreasing at higher carrier densities similar to $1/n_e$ due to phonon scattering in graphene. Eventually, an ultrahigh switching speed of 178 GHz is calculated for the GIG junction [Fig. 9(b)], surpassing the performance of its n-Si–HfO$_2$–ITO counterpart.

Stepping forward to the mapping of the temporal carrier-concentration changes to NIR material permittivity variations, the transient electromagnetic response for both ITO and graphene modulators is calculated. For the case of in-line modulators, the temporal mode loss is directly retrieved by feeding the mode solver with the respective carrier-concentration snapshot. Based on Fig. 10, switching speeds well above 100 GHz are calculated for both ITO and graphene in-line modulators (Table III), with the electromagnetic response proven more susceptible to switching than the gating stimulus [Fig. 9(b)], attributed to the increased sensitivity of the
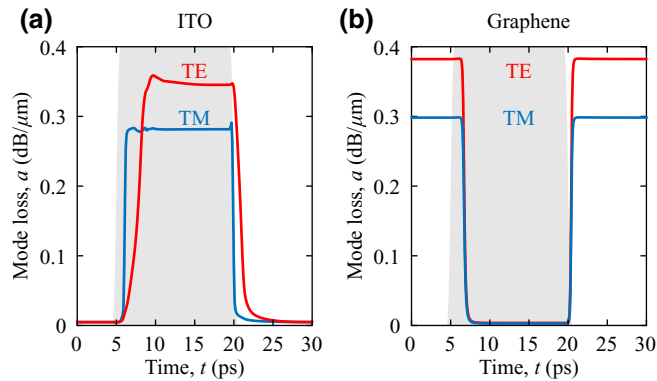

FIG. 10. The mode loss per unit length for (a) ITO and (b) graphene in-line modulators under the application of a 4-V and 2-V rectangular pulse (shaded area), respectively.

underlying NIR phenomena. In contrast to the anticipated polarization-insensitive performance of graphene modulators, TCO designs manifest an over twofold speed difference, with the TM design reaching an impressive 435 GHz speed, greatly outperforming its TE counterpart. For reference, the bandwidth of the applied pulse equals approximately 700 GHz. This can be attributed to the shorter distance between the top electrode and the single ENZ-active interface, allowing for a rapid carrier-concentration settling to the 4-V equilibrium value. In fact, relocating the ground electrode on the side of the ITO layer yields a speed of 162 GHz, close to the TE reported value.

On the other hand, the temporal evaluation of microring modulators requires consideration not only of the inertia of the switching mechanism but also the cavity dynamics, quantified through the photon lifetime. Both effects are evaluated using the temporal CMT framework [50],

$$\frac{d\tilde{\alpha}}{dt} = -j\left[\omega - \omega_{res}(t)\right]\tilde{\alpha} - \left[\frac{1}{\tau_i(t)} + \frac{1}{\tau_e}\right]\tilde{\alpha} + j\sqrt{\frac{2}{\tau_e}}\tilde{s}_{in}, \quad (7a)$$

$$\tilde{s}_{out} = \tilde{s}_{in} + j\sqrt{\frac{2}{\tau_e}}\tilde{\alpha}, \quad (7b)$$

where the slowly varying envelope approximation $\alpha = \tilde{\alpha}(t)\exp(j\omega t)$, $s_{in} = \tilde{s}_{in}(t)\exp(j\omega t)$, $s_{out} = \tilde{s}_{out}(t)\exp(j\omega t)$ is applied for the amplitude of the cavity, input, and output waves, respectively. The external photon lifetime τ_e is considered to be approximately constant. Note that setting $d\tilde{\alpha}/dt = 0$ in Eq. (7a) and substituting in Eq. (7b) results in the steady-state transmission introduced in Eq. (5) of Sec. V.

Introducing a continuous wave ($\tilde{s}_{in} =$ constant) and under the application of a 4-V (2-V) rectangular pulse, the temporal transmission $T(\omega_0, t) \equiv |\tilde{s}_{out}/\tilde{s}_{in}|^2$ for ITO (graphene) microring modulators is illustrated in Fig. 11. The results are compared with the ideal case of instantaneous EO switching, recovered by momentarily assuming a step change for the pertinent parameter values in Eqs. (7). Evidently, the cavity dynamics pose no speed limitation to the response of microring modulators, the bandwidth of which is rather limited by the switching effect. With reference to Table III, ultrahigh switching speeds (> 100 GHz) are achieved by microring designs as well, reduced on average by 34% compared with their respective in-line counterparts—achieved, however, for less than a half of their energy requirements. The electrode configuration between the in-line and microring designs is kept as similar as possible to allow for a direct speed comparison.

To conclude, we emphasize that the performed speed calculations do not account for any contact or external driver resistance. Thus, we present the inherent limitations to the bandwidth of the studied modulators, stemming
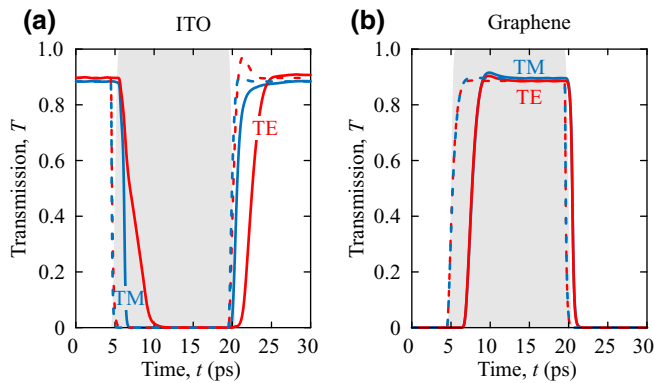
FIG. 11. The temporal transmission for (a) ITO and (b) graphene microring modulators under the application of a 4-V and 2-V rectangular pulse (shaded area), respectively. The dashed lines represent the case of instantaneous EO response, accounting solely for the cavity effect on the response time.

solely from the quality of the constituent materials. The metallic nature of the electrodes is also bound to increase the IL values, especially for the case of TM-polarized waves, due to the excitation of surface plasmon modes. Although this effect is not considered, it can be effectively mitigated by placing the electrodes farther away from the main waveguiding area—accepting, however, a reduction to the overall speed performance.

VII. DISCUSSION

A thorough comparative assessment is presented between the state-of-the-art technologies of TCO and graphene modulators in terms of their IL, footprint, energy consumption, and bandwidth, with the key findings highlighted in this section using Table III. Beginning with the 10-dB in-line modulators, the ITO designs occupy a significantly reduced on-chip area, exhibiting up to 40% reduced footprint in TE operation, despite the calculated greater modulation lengths (Table I). Their losses are slightly higher due to the free-carrier effects in the n-Si core—mitigated, however, by the depletion layers formed under positive bias. Despite their reduced footprint values, they exhibit about fourfold energy requirements due to the n-Si–HfO$_2$–ITO junction calling for a bias swing twice as large as that of the GIG. Both material platforms support impressive switching speeds, well in excess of 100 GHz, with the ITO modulator exhibiting a noteworthy 435 GHz performance in TM operation due to the proximity of the ENZ-active interface to the ground electrode. On the other hand, graphene modulators capitalize on the remarkably high mobility of graphene carriers, far beyond the respective values for conventional semiconductors, to achieve a beneficial compromise between consumption and bandwidth, provided that the sheet width is limited to $w_g \approx 1$ μm ($W_b \propto w_g$, $RC \propto w_g^2$). More sophisticated

physical systems, such as the Si-slot waveguide, could provide enhanced light-matter interaction [15,58], further decreasing the energy requirements.

Next, the microring modulators, which inherently enjoy an infinite ER, are more compact, bending with radii values as small as 1.5 μm. Due to their reduced footprint values, they require less than a half of the energy consumed in their in-line counterparts, with a notable 70% reduction in the case of the ITO microring modulator in TM operation, rendering it competitive over its TE alternative. In all cases, their speed is limited by the dynamics of the switching mechanism to about 34% slower than the respective values for in-line modulators—maintaining, however, an over-100-GHz performance. Overall, the graphene microring modulators are proven most promising, switching for only 0.4 pJ/bit at a speed of almost 200 GHz.

Even though all designs are optimally engineered for both TE and TM operation, the former appears favorable for in-line configurations due to its double-sided (dual-component) interaction with ITO (graphene). This benefit is mitigated in microring modulators by the additional mechanism of radiation loss, which requires suitable engineering of microrings to ensure equivalent modulation performance for both modes of operation. As an overall comparison between in-line and resonant geometries, the former are characterized by ease of fabrication, robustness, and high bandwidth values, whereas the latter stand out for their compactness and energy efficiency. Thus, each modulation scheme should be assessed in accordance with the constraints of the desired application.

Recent results from experimentally demonstrated in-line ITO [59–63] and double-graphene [64–67] modulators indicate that both technologies face challenges related to fabrication issues and suboptimal design, as well as externally applied restrictions. In Fig. 12, an assortment of experimental data are illustrated together with the results of this work (stars). The latter can serve as indicative metrics of ultimate performance, since any comparison with experiment is inequitable. In Fig. 12(a), the total IL for achieving ER = 10 dB is mapped with respect to the required modulation length. Only works with explicitly stated or implicitly inferred IL data are included. The color-shaded regions distinguish between (hybrid) plasmonic and silicon photonic setups, with ITO (graphene) modulators being mostly demonstrated on the former (latter). Strong light-matter interaction in (hybrid) plasmonic modulators allows for micrometer modulation lengths—accompanied, however, with increased IL due to intrinsic ohmic loss. Silicon photonic structures also suffer from high levels of IL, for a multitude of reasons. Suboptimal design hinders efficient light-matter interaction, increasing the required modulation length to hundreds of micrometers, with a detrimental impact on IL. Fabrication challenges related to integration of high-κ dielectrics require settling for insulators of lower dielectric
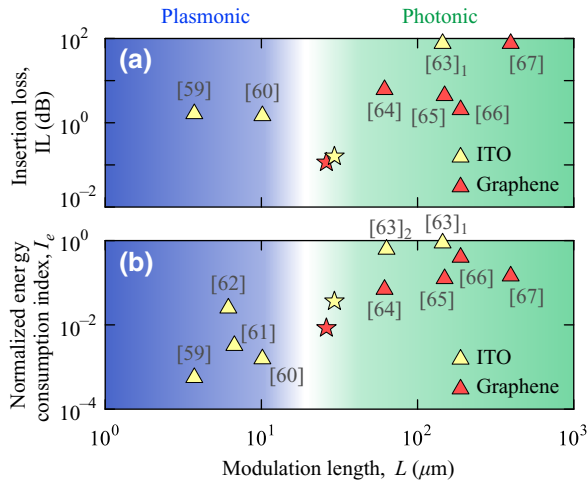
FIG. 12. Experimentally reported results for in-line ITO and double-graphene NIR modulators. (a) The insertion loss and (b) normalized energy consumption index I_e are charted with respect to the required 10-dB modulation length. Both silicon photonic and (hybrid) plasmonic physical systems are evaluated. Two designs are reported in Ref. [63] based on Si-rib and Si-slot waveguides, denoted as [63]$_1$ and [63]$_2$, respectively. The stars correspond to the results of this work.

constant (e.g., Al_2O_3), which scale down the field effect, resulting in an increase of the modulation length as well. A similar effect involves the use of undoped silicon slabs, which introduce a high series resistance, translated into a large voltage drop across silicon. High values of IL also indicate material samples of poor quality, attributed to the demanding multiparametric growth of ITO and graphene, or result from positioning the *on* modulation state in the lossy state of the configurable medium, which boosts ILs and shrinks modulation efficiency.

In Fig. 12(b), an indicative energy-consumption map is presented for the works in Fig. 12(a), including additional available data. The experimental designs are qualitatively evaluated with respect to their energy consumption using the following index:

$$I_e = L \frac{\varepsilon_{\text{static}}}{d} \left[V_{DD}^2 + V_{DD}|V_B| \right], \qquad (8)$$

derived from Ref. [53]. In Eq. (8), L denotes the 10-dB modulation length and $\varepsilon_{\text{static}}$ and d are the dielectric constant and thickness of the insulator, respectively, while $V_{DD} = V_{\text{high}} - V_B$ and $V_B = V_{\text{low}}$ for a bias swing of $[V_{\text{low}}, V_{\text{high}}]$. The results in Fig. 12(b) are normalized to the maximum I_e calculated among both ITO and graphene modulators. Comparing with Fig. 12(a), the energy consumption closely follows the modulation-length trend. Plasmonic modulators exhibit lower energy requirements due to enhanced light-matter interaction (reduced modulation length) and efficient field-effect manifestation (reduced biasing levels). An energy consumption in the

order of picojoule per bit is estimated for double-graphene modulators with Al_2O_3 spacers [64,65]. Thinner layers of higher κ dielectrics would allow for even lower energy consumption values [15].

Gigahertz switching speeds have also been experimentally demonstrated for both ITO (2.5 GHz) [62] and double-graphene modulators (50 GHz) [67], limited by high series resistances due to low carrier mobilities, non-ideal ohmic contacts, and external equipment loads.

Despite the challenges faced, the experimental results on both ITO and graphene modulators are encouraging. The theoretical conclusions of this work suggest that both TCO and graphene platforms hold promise for high-performance modulators with reduced footprint and energy requirements, as well as intrinsic bandwidth values well in excess of 100 GHz. The evaluation of the two material platforms is performed based on a rigorous and consistent modeling of their underlying solid-state and electromagnetic properties, thus serving as a useful and reliable reference for future experimental research.

ACKNOWLEDGMENTS

APPENDIX A: SOLID-STATE PHYSICS ANALYSIS OF ITO AND GRAPHENE JUNCTIONS

Field-effect modeling is systematically described in Ref. [15]. In short, the differential equations for electric charge and current conservation are solved with respect to the electric potential φ and the electron and hole concentrations n and p. The current density is expressed using the drift-diffusion equation, with the carrier concentration following the Fermi-Dirac distribution. Semiconductor-insulator interfaces are conventionally considered free of surface charges, with the normal component of current flow set to zero.

The resulting spatial distribution for the carrier concentration of the 1D n-Si–HfO_2–ITO junction is shown in Fig. 13, originally presented in Ref. [15] and reproduced here for ease of reference. Let us note the critical electron concentration $n_{\text{th}} = 6.11 \times 10^{20}$ cm^{-3}, achieved for a threshold bias $V_{\text{th}} \approx 2.9$ V, coinciding with the onset of the highly lossy state [Fig. 3(a)].

Graphene-comprising junctions are studied in more detail, working toward presenting a straightforward integration of the graphene effect into conventional semiconductor modeling. For this reason, the archetype of a graphene-insulator-metal (GIM) junction is considered in Fig. 14(a), directly generalized for any
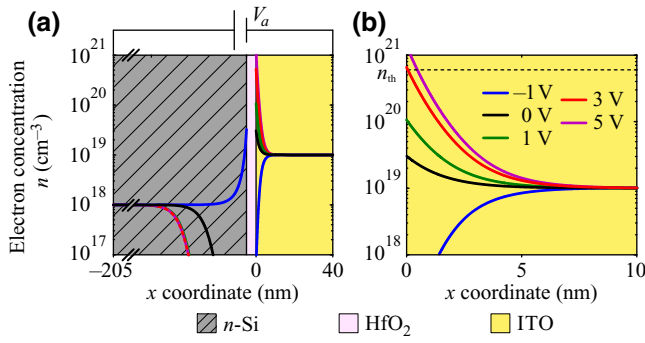
FIG. 13.   (a) The spatial distribution of the electron concentration across the 1D n-Si–HfO$_2$–ITO junction for five biasing values, with the change in concentration for ITO shown in (b). The critical concentration n_{th} manifests itself for $V_a \approx 2.9$ V, maintained for increasing biasing values.

graphene-comprising semiconductor structure. Graphene is electrostatically represented by the boundary condition $\hat{\mathbf{n}} \cdot (\mathbf{D}_G^- - \mathbf{D}_G^+) = \rho_s$, where $\hat{\mathbf{n}}$ is the outward-pointing normal vector, $\mathbf{D}_G^-$ and $\mathbf{D}_G^+$ are the dielectric displacement vectors on each side of the interface, and ρ_s is the surface charge density on graphene.

In general, semiconductor-insulator-semiconductor junctions result in heterogeneous capacitors with plates of different density-of-states (DOS) values. This DOS discrepancy becomes significantly pronounced in structures comprising low-dimensional materials, such as graphene, due to the band-filling effect. Specifically, the low DOS in graphene forces the extra carriers injected during charging to occupy increasingly higher energies, in compliance with Pauli blocking. On the contrary, the high DOS in metals allows a hypothetically infinite number of carriers to occupy the same energy level. As a result, although the electrostatic potential appears constant in metals, it exhibits a discontinuity equal to $|\mu_c|/e$ at the graphene sheet, with μ_c expressing the internal chemical potential change, calculated with respect to the shift of the total

electrostatic potential φ. The internal energy change μ_c in graphene adds to the field energy developed in the insulator to yield the total stored energy in the structure. The two energy contributions are represented through a pair of series capacitances C_q and C_g [Fig. 14(a)], with the former introducing the *quantum capacitance* of graphene and the latter expressing the classical geometry-dependent capacitance [56,68].

In Figs. 14(b)–14(e), the energy-band diagram of the GIM junction is illustrated under different biasing conditions. The 5-nm insulating material is considered to be HfO$_2$ of static dielectric constant $\bar{\varepsilon}_{ins}/\varepsilon_0 = 25$ [40], while the metal contact is set to be Au. The Au work function equals $eW_m = 5.1$ eV, with the respective value for graphene set to $eW_g = 4.5$ eV. In the absence of galvanic contact between the capacitor plates [Fig. 14(b)], their Fermi levels E_f lie below the vacuum energy level E_0 by the respective work-function value. Once a galvanic connection is settled and equilibrium conditions are established [Fig. 14(c)], the Fermi levels are aligned at a common energy level, defined hereafter as the reference level E_{ref}, for calculating the electron potential energy $E_0 - E_{ref} = -e\varphi$. A built-in potential $V_{bi} = 0.6$ V is formed as a result of the work-function mismatch between the capacitor plates. The electric field generated in the insulator forces the energy bands to bend, promoting the charge accumulation, which is equal and opposite in sign on each plate. The capacitor charge can be regulated by applying a positive or negative potential V_a on graphene, shifting its Fermi level by $-eV_a$ as illustrated in Figs. 14(d) and 14(e), respectively. The Fermi level at the ground contact is invariant, coinciding with E_{ref}.

The charge density developed on the graphene sheet equals $\rho_s = -en_s$, with n_s denoting the net carrier density between electrons and holes [69],

$$n_s = \frac{2}{\pi \hbar^2 v_F^2} \int_0^\infty \epsilon \left[f_d(\epsilon) - f_d(\epsilon + 2\mu_c) \right] d\epsilon, \quad \text{(A1)}$$
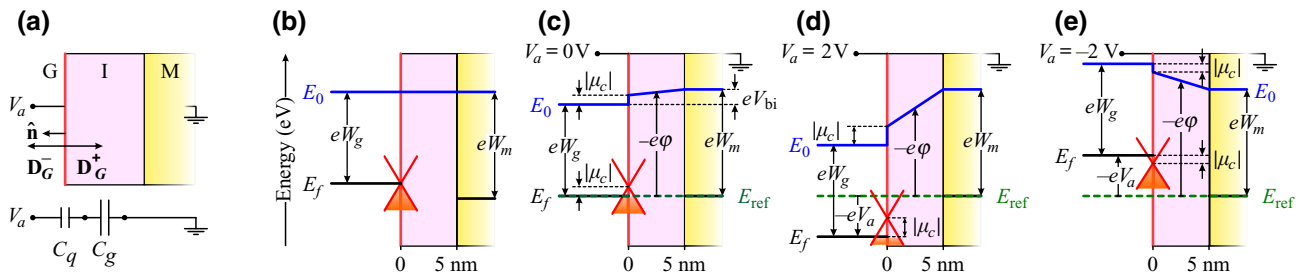

FIG. 14.   (a) The GIM junction under bias, with the graphene charge density ρ_s introduced through $\hat{\mathbf{n}} \cdot (\mathbf{D}_G^- - \mathbf{D}_G^+) = \rho_s$. The electric circuit equivalent, composed of the series capacitances C_q and C_g, is shown at the foot. (b) The energy-band diagram across the GIM junction in the absence of any galvanic contact. (c)–(e) The GIM junction under zero, positive, and negative bias, respectively. The 5-nm insulator is considered to be HfO$_2$, while Au is selected for the metal contact. The chemical potential change μ_c in graphene can be calculated through the change in total electrostatic potential φ.

calculated using the Fermi-Dirac distribution f_d, with the chemical potential μ_c representing the shift of carrier energy with respect to the charge neutral Dirac point, as schematically illustrated using the Dirac cones in Figs. 14(b)–14(e).

In Eq. (A1), the energy level at the Dirac point is considered equal to zero, with positive (negative) chemical potential values resulting in an electron (hole) accumulation. Safely assuming that $|\mu_c| \gg k_B T$ at $T = 300$ K, Eq. (A1) can be simplified to $n_s \approx \text{sign}(\mu_c)\mu_c^2/\pi\hbar^2 v_F^2$. With reference to Figs. 14(c)–14(e), the chemical potential can be expressed in terms of the total electrostatic potential as $\mu_c = e(W_g - V_a + \varphi)$, obtaining positive (negative) values in the case of electron (hole) accumulation, with V_a denoting the signed value of the applied bias. Eventually, the charge density on graphene is given by

$$\rho_s = -e\,\text{sign}(W_g - V_a + \varphi)\frac{[e(W_g - V_a + \varphi)]^2}{\pi\hbar^2 v_F^2}. \quad \text{(A2)}$$

Consequently, the interface condition for the dielectric displacement $\hat{\mathbf{n}} \cdot (\mathbf{D}_G^- - \mathbf{D}_G^+) = \rho_s$ can be rewritten in a Neumann-type boundary condition as

$$\nabla\varphi \cdot \hat{\mathbf{n}} = -\frac{e}{\bar{\varepsilon}_{\text{ins}}}\text{sign}(W_g - V_a + \varphi)\frac{[e(W_g - V_a + \varphi)]^2}{\pi\hbar^2 v_F^2}, \quad \text{(A3)}$$

since $\mathbf{D}_G^- = \mathbf{0}$ and $\mathbf{D}_G^+ = \bar{\varepsilon}_{\text{ins}}\mathbf{E}_G^+ = -\bar{\varepsilon}_{\text{ins}}\nabla\varphi$, thus resulting in a universal expression for introducing the electrostatic graphene effect into semiconductor modeling and enabling a straightforward and fair comparison between graphene modulators of arbitrary geometry (Appendix B).

In Fig. 15, the described modeling framework is applied to three practical cases of graphene-comprising junctions—i.e., the already presented GIM, the graphene-insulator-semiconductor (GIS), and the GIG structure—to illustrate the chemical potential change in graphene as a function of the applied bias (solid lines). The considered metal, semiconductor, and insulator materials are Au, n-doped (10^{18} cm^{-3}) silicon, and HfO$_2$, respectively. The colored markers in Figs. 15(a)–15(c) result from equivalent electric circuit calculations based on the closed-form relations

$$V_{a,\text{GIM}} = V_{\text{bi}} + \mu_c/e + V_{\text{ins}}, \quad \text{(A4a)}$$

$$V_{a,\text{GIS}} = V_{\text{bi}} + \mu_c/e + V_{\text{ins}} + V_{\text{semi}}, \quad \text{(A4b)}$$

$$V_{a,\text{GIG}} = V_{\text{bi}} + \mu_c/e + V_{\text{ins}} + \mu_c/e, \quad \text{(A4c)}$$

and are in excellent agreement with the solid-line semiconductor simulations. In Eq. (A4), the applied bias at each junction is decomposed into its components, including voltage drops V_{ins} and V_{semi} across the insulator and semiconductor parts, respectively, calculated
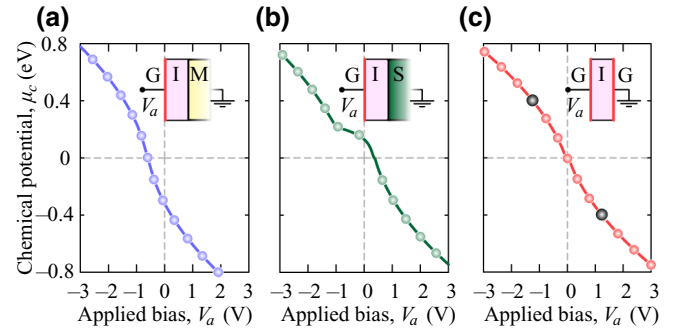

FIG. 15. The chemical potential change in graphene as a function of V_a for three practical graphene junctions: (a) graphene-insulator-metal, (b) graphene-insulator-semiconductor, and (c) graphene-insulator-graphene. The solid lines result from semiconductor simulations, while the colored markers correspond to equivalent electric circuit calculations. For the GIG junction, $|\mu_{c,\text{th}}| = 0.4$ eV at $|V_{\text{th}}| \approx 1.2$ V (black markers).

using $V_{\text{ins}} = Q/C_g$ and the semiconductor capacitance $C_{\text{semi}} = \partial Q/\partial V_{\text{semi}}$, accordingly.

For the GIG junction, the critical value $|\mu_{c,\text{th}}| = 0.4$ eV is achieved at $|V_{\text{th}}| \approx 1.2$ V (black markers), coinciding with the loss drop in Fig. 3(b). The symmetric change with respect to zero bias evidenced in Fig. 15(c) is attributed to the equal work-function values considered for both graphene sheets ($V_{\text{bi}} = 0$).

APPENDIX B: SINGLE-GRAPHENE MODULATORS

In Fig. 16, single-graphene designs are compared with their double-graphene counterpart employed in Sec. IV and we arrive at the conclusion that a pair of graphene monolayers separated by a high-κ dielectric is the most promising and fabrication-friendly configuration for effectively controlling the optical conductivity of graphene by means of the field effect.

Specifically, in Figs. 16(a) and 16(b), an Si-rib waveguide is loaded with a graphene monolayer in sheet and nanoribbon geometry, respectively, lying on top of an HfO$_2$ layer and spaced 5 nm from the underlying n-Si core. The waveguide dimensions $w \times h = 400 \times 120$ nm^2 coincide with the respective values for the optimized double-graphene modulator of Sec. IV in TE operation. An unetched 30-nm slab serves as an electrical access to the n-Si core. In Fig. 16(c), graphene conformally covers n-Si, being electrically isolated from it by an intermediate 5-nm HfO$_2$ spacer. In this geometry, the HfO$_2$ cladding is maintained to ensure a direct comparison with the designs in Figs. 16(a) and 16(b)—in principle, however, being redundant. In single-graphene designs, the graphene conductivity is modulated by the electric field developed in HfO$_2$ as a result of the applied bias between n-Si and
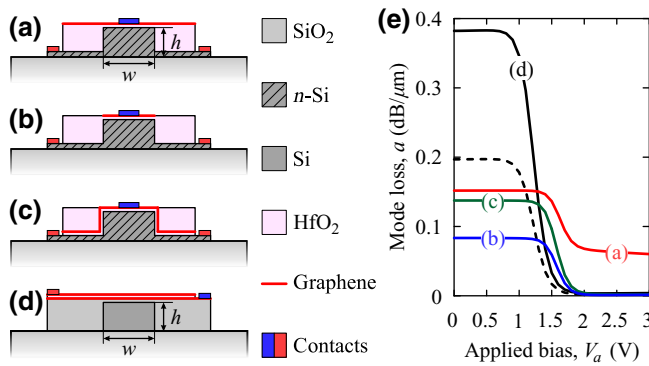
FIG. 16. (a)–(c) Single-graphene modulators, with the bias applied between the n-Si slab and graphene. The thickness of the unetched slab equals 30 nm, while $w \times h = 400 \times 120$ nm^2. (a) Graphene sheet and (b) graphene nanoribbon lying on top of an HfO$_2$ layer, spaced 5 nm from the underlying n-Si core. (c) Graphene conformally covering n-Si above a 5-nm HfO$_2$ spacer. (d) The double-graphene modulator. (e) The mode loss in TE operation for the designs in (a)–(d) as a function of V_a. The dashed line represents the loss introduced by the equivalent single-graphene design of (d) after artificially switching off the induced current density on the upper graphene sheet.

graphene. The field effect is introduced using the mathematical framework described in Appendix A.

In Fig. 16(e), the TE-mode loss in single-graphene designs is illustrated as a function of the applied bias, compared with the respective value for the double-graphene modulator in Fig. 16(d). The simplest design in Fig. 16(a) achieves an ER value of merely 0.09 dB/μm by toggling between the unbiased state and 3 V, calling for a 10-dB modulation length exceeding 100 μm, with the respective IL surpassing 6 dB. Such a poor performance is attributed to the nonuniform chemical potential change along the graphene sheet due to the decreasing field-effect strength on each side of the Si core, originating from the increase in the HfO$_2$ thickness. As a result, graphene fails to cross the $\mu_{c,\mathrm{th}}$ threshold beyond the Si-core region, remaining lossy in the biased state and thus shrinking the attainable ER.

This geometric deficiency is alleviated in Fig. 16(b) by restricting the graphene sheet to a w-width nanoribbon, centered around the Si core. Truly, as evidenced in Fig. 16(e), the mode loss drops significantly at 3 V, with an inevitable drop in the unbiased state as well, after the effect of the reduction in the overall light-graphene interaction. Even though ER is restricted to 0.08 dB/μm, the total IL for a 10-dB modulation length is significantly reduced to 0.20 dB. An even more improved performance (ER = 0.14 dB/μm, IL = 0.10 dB) can be achieved with the design in Fig. 16(c) by allowing graphene to follow the waveguide outline, ensuring both a uniform change in its chemical potential and an enhanced interaction with the guided mode, as evidenced in Figs. 4(a) and 4(c).

However, the most practical graphene devices envisioned at this time should integrate graphene as an unprocessed planar sheet, ideally lying on top of the structure to maintain increased carrier mobility. Consequently, the alternatives presented in Figs. 16(b) and 16(c) are almost impractical from a fabrication standpoint. Specifically, the design in Fig. 16(b) employs nanoribbons of graphene, accurately aligned with the underlying Si core, which is significantly challenging especially in the case of ring resonators, while the formation of graphene edges introduces additional physical effects. On the other hand, the design in Fig. 16(c) can be solely investigated as a theoretical case study, since a graphene sheet conformally following the sharp waveguide edges appears unrealistic and impractical.

Thus, the parallel configuration of graphene monolayers in Fig. 16(d) succeeds in compromising the need for efficient field-effect changes with fabrication feasibility. In addition, it exhibits enhanced modulation performance compared to single-graphene modulators due to the twofold graphene effect [Fig. 16(e)]. A more straightforward comparison results from artificially switching off the induced current density on the upper graphene sheet (dashed line), deriving an equivalent single-graphene configuration with a uniform chemical potential change. The respective loss is represented by the dashed line in Fig. 16(e), resulting in ER $\approx$ 0.20 dB/μm and a total IL of 0.10 dB after a 10-dB modulation length, surpassing the performance of its single-graphene counterparts. Moreover, the double-graphene modulator in Fig. 16(d) employs an intrinsic silicon waveguide instead of the n-doped slab of Figs. 16(a)–16(c), avoiding the lossy free-carrier effects in n-Si, even though the latter are not considered in the calculations of Fig. 16(e) solely to illustrate the graphene effect. Furthermore, the GIG junction is favorable in terms of bandwidth and energy consumption compared to its GIS counterpart, with the V_{th} values estimated to be around 1.2 V and 1.6 V, respectively, complying with the 1D calculations in Figs. 15(b) and 15(c).

[1] Y. Enami, C. T. Derose, D. Mathine, C. Loychik, C. Green-lee, R. A. Norwood, T. D. Kim, J. Luo, Y. Tian, A. K.-Y. Jen, and N. Peyghambarian, Hybrid polymer/sol-gel waveguide modulators with exceptionally large electrooptic coefficients, Nat. Photonics **1**, 180 (2007).

[2] M. Wuttig, H. Bhaskaran, and T. Taubner, Phase-change materials for non-volatile photonic applications, Nat. Photonics **11**, 465 (2017).

[3] Z. Sun, A. Martinez, and F. Wang, Optical modulators with 2D layered materials, Nat. Photonics **10**, 227 (2016).

[4] X. Liu, Q. Guo, and J. Qiu, Emerging low-dimensional materials for nonlinear optics and ultrafast photonics, Adv. Mater. **29**, 1605886 (2017).

[5] V. E. Babicheva, N. Kinsey, G. V. Naik, M. Ferrera, A. V. Lavrinenko, V. M. Shalaev, and A. Boltasseva, Towards CMOS-compatible nanophotonics: Ultra-compact

modulators using alternative plasmonic materials, Opt. Express **21**, 27326 (2013).

[6] V. E. Babicheva, A. Boltasseva, and A. V. Lavrinenko, Transparent conducting oxides for electro-optical plasmonic modulators, Nanophotonics **4**, 165 (2015).

[7] Q. Gao, E. Li, and A. X. Wang, Comparative analysis of transparent conductive oxide electro-absorption modulators [invited], Opt. Mater. Express **8**, 2850 (2018).

[8] S. Luo, Y. Wang, X. Tong, and Z. Wang, Graphene-based optical modulators, Nanoscale Res. Lett. **10**, 199 (2015).

[9] M. Romagnoli, V. Sorianello, M. Midrio, F. H. L. Koppens, C. Huyghebaert, D. Neumaier, P. Galli, W. Templ, A. D'Errico, and A. C. Ferrari, Graphene-based integrated photonics for next-generation datacom and telecom, Nat. Rev. Mater. **3**, 392 (2018).

[10] K. Ellmer, Past achievements and future challenges in the development of optically transparent electrodes, Nat. Photonics **6**, 809 (2012).

[11] E. Feigenbaum, K. Diest, and H. A. Atwater, Unity-order index change in transparent conducting oxides at visible frequencies, Nano Lett. **10**, 2111 (2010).

[12] J. Park, J.-H. Kang, X. Liu, and M. L. Brongersma, Electrically tunable epsilon-near-zero (ENZ) metafilm absorbers, Sci. Rep. **5**, 15754 (2015).

[13] D. C. Zografopoulos, G. Sinatkas, E. Lotfi, L. A. Shahada, M. A. Swillam, E. E. Kriezis, and R. Beccherelli, Amplitude modulation in infrared metamaterial absorbers based on electro-optically tunable conducting oxides, Appl. Phys. A **124**, 105 (2018).

[14] A. P. Vasudev, J.-H. Kang, J. Park, X. Liu, and M. L. Brongersma, Electro-optical modulation of a silicon waveguide with an epsilon-near-zero material, Opt. Express **21**, 26387 (2013).

[15] G. Sinatkas, A. Pitilakis, D. C. Zografopoulos, R. Beccherelli, and E. E. Kriezis, Transparent conducting oxide electro-optic modulators on silicon platforms: A comprehensive study based on the drift-diffusion semiconductor model, J. Appl. Phys. **121**, 023109 (2017).

[16] A. Melikyan, N. Lindenmann, S. Walheim, P. M. Leufke, S. Ulrich, J. Ye, P. Vincze, H. Hahn, T. Schimmel, C. Koos, W. Freude, and J. Leuthold, Surface plasmon polariton absorption modulator, Opt. Express **19**, 8855 (2011).

[17] A. V. Krasavin and A. V. Zayats, Photonic Signal Processing on Electronic Scales: Electro-Optical Field-Effect Nanoplasmonic Modulator, Phys. Rev. Lett. **109**, 053901 (2012).

[18] D. C. Zografopoulos and K. P. Prokopidis, Transparent Nanoprobes in Integrated Plasmonic Circuits Based on Plasmonic Cloaking, Phys. Rev. Appl. **2**, 064009 (2014).

[19] C. Lin and A. S. Helmy, Dynamically reconfigurable nanoscale modulators utilizing coupled hybrid plasmonics, Sci. Rep. **5**, 12313 (2015).

[20] U. Koch, C. Hoessbacher, J. Niegemann, C. Hafner, and J. Leuthold, Digital plasmonic absorption modulator exploiting epsilon-near-zero in transparent conducting oxides, IEEE Photonics J. **8**, 4800813 (2016).

[21] L. Tao, A. Anopchenko, S. Gurung, J. Zhang, and H. W. H. Lee, Gate-tunable plasmon-induced transparency modulator based on stub-resonator waveguide with epsilon-near-zero materials, Sci. Rep. **9**, 2789 (2019).

[22] A. K. Geim and K. S. Novoselov, The rise of graphene, Nat. Mater. **6**, 183 (2007).

[23] M. Liu, X. Yin, E. Ulin-Avila, B. Geng, T. Zentgraf, L. Ju, F. Wang, and X. Zhang, A graphene-based broadband optical modulator, Nature **474**, 64 (2011).

[24] Y. Hu, M. Pantouvaki, J. V. Campenhout, S. Brems, I. Asselberghs, C. Huyghebaert, P. Absil, and D. V. Thourhout, Broadband 10 Gb/s operation of graphene electro-absorption modulator on silicon, Laser Photon. Rev. **10**, 307 (2016).

[25] V. Sorianello, M. Midrio, G. Contestabile, I. Asselberghs, J. V. Campenhout, C. Huyghebaert, I. Goykhman, A. K. Ott, A. C. Ferrari, and M. Romagnoli, Graphenesilicon phase modulators with gigahertz bandwidth, Nat. Photonics **12**, 40 (2017).

[26] S. J. Koester and M. Li, High-speed waveguide-coupled graphene-on-graphene optical modulators, Appl. Phys. Lett. **100**, 171107 (2012).

[27] V. Sorianello, M. Midrio, and M. Romagnoli, Design optimization of single and double layer graphene phase modulators in SOI, Opt. Express. **23**, 6478 (2015).

[28] Y. Kim and M.-S. Kwon, Electroabsorption modulator based on inverted-rib-type silicon waveguide including double graphene layers, J. Opt. **19**, 045804 (2017).

[29] Z. Ma, Z. Li, K. Liu, C. Ye, and V. J. Sorger, Indium-tin-oxide for high-performance electro-optic modulation, Nanophotonics **4**, 198 (2015).

[30] S. Zhu, G. Q. Lo, and D. L. Kwong, Electro-absorption modulation in horizontal metal-insulator-silicon-insulator-metal nanoplasmonic slot waveguides, Appl. Phys. Lett. **99**, 151114 (2011).

[31] Z. Lu, W. Zhao, and K. Shi, Ultracompact electroabsorption modulators based on tunable epsilon-near-zero-slot waveguides, IEEE Photonics J. **4**, 735 (2012).

[32] D. Chatzidimitriou, A. Pitilakis, and E. E. Kriezis, Rigorous calculation of nonlinear parameters in graphene-comprising waveguides, J. Appl. Phys. **118**, 023105 (2015).

[33] G. W. Hanson, Dyadic Green's functions and guided surface waves for a surface conductivity model of graphene, J. Appl. Phys. **103**, 064302 (2008).

[34] L. A. Falkovsky and A. A. Varlamov, Space-time dispersion of graphene conductivity, The European Physical Journal B **56**, 281 (2007).

[35] Y.-C. Chang, C.-H. Liu, C.-H. Liu, Z. Zhong, and T. B. Norris, Extracting the complex optical conductivity of mono- and bilayer graphene by ellipsometry, Appl. Phys. Lett. **104**, 261909 (2014).

[36] Y.-W. Tan, Y. Zhang, K. Bolotin, Y. Zhao, S. Adam, E. H. Hwang, S. DasSarma, H. L. Stormer, and P. Kim, Measurement of Scattering Rate and Minimum Conductivity in Graphene, Phys. Rev. Lett. **99**, 246803 (2007).

[37] M. Breusing, C. Ropers, and T. Elsaesser, Ultrafast Carrier Dynamics in Graphite, Phys. Rev. Lett. **102**, 086809 (2009).

[38] J. M. Dawlaty, S. Shivaraman, M. Chandrashekhar, F. Rana, and M. G. Spencer, Measurement of ultrafast carrier dynamics in epitaxial graphene, Appl. Phys. Lett. **92**, 042116 (2008).

[39] L. A. Falkovsky, Optical properties of doped graphene layers, Journal of Experimental and Theoretical Physics **106**, 575 (2008).

[40] G. D. Wilk, R. M. Wallace, and J. M. Anthony, High-κ gate dielectrics: Current status and materials properties considerations, J. Appl. Phys. **89**, 5243 (2001).

[41] R. Amin, C. Suer, Z. Ma, I. Sarpkaya, J. B. Khurgin, R. Agarwal, and V. J. Sorger, Active material, optical mode and cavity impact on nanoscale electro-optic modulation performance, Nanophotonics **7**, 455 (2017).

[42] C. T. Phare, Y.-H. D. Lee, J. Cardenas, and M. Lipson, Graphene electro-optic modulator with 300 GHz bandwidth, Nat. Photonics **9**, 511 (2015).

[43] M. Midrio, S. Boscolo, M. Moresco, M. Romagnoli, C. D. Angelis, A. Locatelli, and A.-D. Capobianco, Graphene-assisted critically-coupled optical ring modulator, Opt. Express. **20**, 23144 (2012).

[44] E. Li, B. A. Nia, B. Zhou, and A. X. Wang, Transparent conductive oxide-gated silicon microring with extreme resonance wavelength tunability, Photonics Research **7**, 473 (2019).

[45] G. Isic, G. Sinatkas, D. C. Zografopoulos, B. Vasic, A. Ferraro, R. Beccherelli, E. E. Kriezis, and M. Belic, Electrically tunable metal-semiconductor-metal terahertz metasurface modulators, IEEE. J. Sel. Top. Quantum. Electron. **25**, 8500108 (2019).

[46] J. B. Pendry, Controlling electromagnetic fields, Science **312**, 1780 (2006).

[47] D. M. Shyroki, Exact equivalent straight waveguide model for bent and twisted waveguides, IEEE. Trans. Microw. Theory. Tech. **56**, 414 (2008).

[48] Z. Han, P. Zhang, and S. I. Bozhevolnyi, Calculation of bending losses for highly confined modes of optical waveguides with transformation optics, Opt. Lett. **38**, 1778 (2013).

[49] W. Bogaerts, P. D. Heyn, T. V. Vaerenbergh, K. D. Vos, S. K. Selvaraja, T. Claes, P. Dumon, P. Bienstman, D. V. Thourhout, and R. Baets, Silicon microring resonators, Laser Photonics Rev. **6**, 47 (2011).

[50] B. Little, S. Chu, H. Haus, J. Foresi, and J.-P. Laine, Microring resonator channel dropping filters, J. Lightwave Technol. **15**, 998 (1997).

[51] T. Christopoulos, O. Tsilipakos, N. Grivas, and E. E. Kriezis, Coupled-mode-theory framework for nonlinear resonators comprising graphene, Phys. Rev. E **94**, 062219 (2016).

[52] O. Tsilipakos, T. Christopoulos, and E. E. Kriezis, Long-range hybrid plasmonic disk resonators for mW bistability and self-pulsation, J. Lightwave Technol. **34**, 1333 (2016).

[53] D. A. B. Miller, Energy consumption in optical modulators for interconnects, Opt. Express **20**, A293 (2012).

[54] G. Sinatkas and E. E. Kriezis, Silicon-photonic electro-optic phase modulators integrating transparent conducting oxides, IEEE J. Quantum Electron. **54**, 8400208 (2018).

[55] J.-M. Sallese, A new constituent of electrostatic energy in semiconductors, Eur. Phys. J. B **89**, 136 (2016).

[56] T. Fang, A. Konar, H. Xing, and D. Jena, Carrier statistics and quantum capacitance of graphene sheets and ribbons, Appl. Phys. Lett. **91**, 092109 (2007).

[57] K. Zou, X. Hong, D. Keefer, and J. Zhu, Deposition of High-Quality HfO_2 on Graphene and the Effect of Remote Oxide Phonon Scattering, Phys. Rev. Lett. **105**, 126601 (2010).

[58] T. Christopoulos, O. Tsilipakos, and E. E. Kriezis, Low-power bistability in graphene-comprising 3D photonic resonant circuits, J. Appl. Phys. **122**, 233101 (2017).

[59] H. W. Lee, G. Papadakis, S. P. Burgos, K. Chander, A. Kriesch, R. Pala, U. Peschel, and H. A. Atwater, Nanoscale conducting oxide PlasMOStor, Nano Lett. **14**, 6463 (2014).

[60] V. J. Sorger, N. D. Lanzillotti-Kimura, R.-M. Ma, and X. Zhang, Ultra-compact silicon nanophotonic modulator with broadband response, Nanophotonics **1**, 17 (2012).

[61] Q. Gao, E. Li, and A. X. Wang, Ultra-compact and broadband electro-absorption modulator using an epsilon-near-zero conductive oxide, Photonics Res. **6**, 277 (2018).

[62] M. G. Wood, S. Campione, S. Parameswaran, T. S. Luk, J. R. Wendt, D. K. Serkland, and G. A. Keeler, Gigahertz speed operation of epsilon-near-zero silicon photonic modulators, Optica **5**, 233 (2018).

[63] X. Liu, K. Zang, J.-H. Kang, J. Park, J. S. Harris, P. G. Kik, and M. L. Brongersma, Epsilon-near-zero Si slot-waveguide modulator, ACS Photonics **5**, 4484 (2018).

[64] M. Liu, X. Yin, and X. Zhang, Double-layer graphene optical modulator, Nano Lett. **12**, 1482 (2012).

[65] H. Dalir, Y. Xia, Y. Wang, and X. Zhang, Athermal broadband graphene optical modulator with 35 GHz speed, ACS Photonics **3**, 1564 (2016).

[66] M. Mohsin, D. Schall, M. Otto, A. Noculak, D. Neumaier, and H. Kurz, Graphene based low insertion loss electro-absorption modulator on SOI waveguide, Opt. Express **22**, 15292 (2014).

[67] M. A. Giambra, V. Sorianello, V. Miseikis, S. Marconi, A. Montanaro, P. Galli, S. Pezzini, C. Coletti, and M. Romagnoli, High-speed double layer graphene electro-absorption modulator on SOI waveguide, Opt. Express **27**, 20145 (2019).

[68] J. Fernández-Rossier, J. J. Palacios, and L. Brey, Electronic structure of gated graphene and graphene ribbons, Phys. Rev. B **75**, 205441 (2007).

[69] G. W. Hanson, Dyadic Green's functions for an anisotropic, non-local model of biased graphene, IEEE Trans. Antennas Propag. **56**, 747 (2008).